sustainability

MDPI

Article

Mechanical Properties and Drying Shrinkage of Alkali-Activated Coal Gangue Concrete

Yanbing Zhao [1], Caiqian Yang [1,2,*], Feng Qu [1], Kefeng Li [1,2], Jing Yang [3] and Zhiren Wu [4,*]

[1] Key Laboratory of Concrete and Prestressed Concrete Structures of Ministry of Education, Southeast University, Nanjing 210096, China
[2] Jiangsu ZYZ Intelligent Operation & Maintenance Institute, Nanjing 210003, China
[3] College of Architectural Science and Engineering, Yangzhou University, Yangzhou 225127, China
[4] School of the Environment and Safety Engineering, Jiangsu University, Zhenjiang 212013, China
* Correspondence: ycqjxx@seu.edu.cn (C.Y.); wwu5353@j-c-k.co.jp (Z.W.)

Abstract: The feasibility of composite-activated coal gangue (CACG) as the primary cementitious material for concrete was experimentally studied in this paper. The effects of concrete strength grade on slump and slump flow, compressive strength, splitting tensile strength, axial compressive strength, elastic modulus, and drying shrinkage of alkali-activated coal gangue concrete (AACGC) were experimentally investigated. Experimental results indicated that the slump and slump flow of the AACGC were smaller than that of ordinary Portland cement concrete (OPCC). The mechanical properties of the AACGC were superior to those of the OPCC. The compressive strength, splitting tensile strength, axial compressive strength, and elastic modulus of the AACGC were 1.17 times, 1.04 times, 1.47 times, and 1.04 times those of the OPCC, respectively. With the increase in concrete strength grade, the mechanical properties of the AACGC have gradually increased. The difference in failure modes of axial compressive strength between the AACGC and OPCC was analyzed. Moreover, the empirical formulas of the elastic modulus and compressive strength for the OPCC in various regions codes were summarized, and found that the empirical formula in GB 50010-2002 code and EN 1922 Eurocode 2 was also applicable to the AACGC. Finally, the mass-loss rate and drying shrinkage for the AACGC at different concrete strength grades were systematically analyzed, and a hyperbolic prediction model was proposed to reflect the drying shrinkage behavior of the AACGC.

Keywords: coal gangue; alkali-activated coal gangue concrete; mechanical properties; drying shrinkage

check for updates

Citation: Zhao, Y.; Yang, C.; Qu, F.; Li, K.; Yang, J.; Wu, Z. Mechanical Properties and Drying Shrinkage of Alkali-Activated Coal Gangue Concrete. *Sustainability* **2022**, *14*, 14736. https://doi.org/10.3390/su142214736

Academic Editor: Jonathan Oti

Received: 30 September 2022
Accepted: 2 November 2022
Published: 9 November 2022

1. Introduction

Coal gangue was the main by-product of the coal mining and washing industries, and it is one of the most massive industrial wastes worldwide. It was reported that coal gangue accounts for about 15~20% of the coal output, and its emission exceeds 7 billion tons, with an annual increase rate of 150 million tons in China [1,2]. Over time, such non-biodegradable wastes occupy land, pollute the environment by processes such as air pollution and heavy metal erosion in water and soil, and even induce geological disasters [3,4]. Hence, the utilization of coal gangue as a recyclable resource has become a global issue [5–8].

With the rapid development of the construction industry, the consumption of ordinary Portland cement (OPC) has increased significantly, resulting in an increasing shortage of non-renewable clay resources. In addition, every ton of OPC produced will emit 800~1000 kg of carbon dioxide into the atmosphere [9,10]. Therefore, the search for cementitious materials with low energy, low resource consumption, and low carbon footprint has become the focus of current research. In 1940, Purdon first proposed that sodium hydroxide could be used to activate the reactivity of pozzolanic materials (such as slag, fly ash, and coal gangue) in order to prepare alkali-activated cementitious materials (AACM) [11]. Subsequently, researchers found that the AACM exhibited superior performance, including

dense microstructure, high early strength, low heat of hydration, and excellent resistance to chemical attack [12–14]. Therefore, the AACM is considered an environment-friendly substitute for the OPC for the purpose of achieving efficient industrial solid waste recycling. Meanwhile, it was reported that the main chemical compositions of coal gangue were aluminum oxide (Al_2O_3) and silicon dioxide (SiO_2), accounting for more than 80% of the total, which was similar to fly ash [8]. Consequently, it may be a potential green cementitious material, which can entirely or partially replace ordinary Portland cement in the construction industry. In addition, coal gangue has more reserves, higher content of silica and alumina, and higher cementitious material activity compared to metallurgical wastes, such as steel slag, red mud, and copper slag.

Coal gangue can be viewed as a potential resource instead of a waste after appropriate treatment. Some researchers have adopted coal gangue treated by mechanical activation or thermal activation as an admixture in concrete [15,16]. However, the proportion of coal gangue in cementitious materials was still less than 15% due to its low reactivity [17,18]. In order to increase and accelerate the utilization of coal gangue, researchers began to investigate the feasibility of using coal gangue to prepare alkali-activated coal gangue cementitious materials. Zhang et al. found [19] that sodium silicate could generate more hydration productions in comparison with sodium hydroxide and potassium hydroxide for alkali-activated coal gangue cementitious materials. Zhao et al. [20] adopted the composite-activated coal gangue to prepare alkali-activated coal gangue cementitious materials. They also analyzed the influencing factors of compressive strength, including the modulus of sodium silicate, alkali content, calcination temperature, holding time, and water-to-binder ratio. Ma et al. [21–23] investigated the mechanical properties, drying shrinkage, and durability of alkali-activated coal gangue mortar. Currently, relevant research mainly focuses on the activation method and mechanism of coal gangue, factors influencing the activity of coal gangue and its mechanism, the hydration mechanism of alkali-activated coal gangue cementitious materials, and the workability, mechanical properties, microstructure characteristics, chloride ion penetration, and durability of alkali-activated coal gangue mortars. However, few investigations have focused on the mechanical properties, failure modes, ratio of splitting tensile strength to compressive strength, conversion formula between elastic modulus, and compressive strength of alkali-activated coal gangue concrete (AACGC). Although many researchers have shown that the drying shrinkage of alkali-activated materials is higher than that of cement-based materials [23–25], the research on the drying shrinkage behavior and prediction model of the AACGC is still insufficient.

In this paper, the composite-activated coal gangue (CACG) was employed as a primary cementitious material to fabricate the AACGC. Three concrete strength grades (C30, C40, and C50) were designed to systematically investigate the workability, mechanical properties, and drying shrinkage of AACGC at various curing ages. The differences in the slump and slump flow, compressive strength, splitting tensile strength, elastic modulus, axial compressive strength, and failure modes of the AACGC and ordinary Portland cement concrete (OPCC) were compared and analyzed. Moreover, the empirical formulas of the elastic modulus and compressive strength for the OPCC in various regions codes were summarized and applied to the AACGC. Finally, the effects of concrete strength grade on drying shrinkage of the AACGC were systematically analyzed, and a hyperbolic prediction model was proposed to reflect the drying shrinkage behavior of the AACGC.

2. Experimental Section

2.1. Raw Materials

The raw coal gangue samples were mined from the Ordos area of the Inner Mongolia Ordos region of China. In addition, the S95 grade granulated blast furnace slag was used as a supplementary cementitious material, the specific surface area and density of which were 450 m^2/kg and 2.9 g/cm^3, respectively. Ordinary Portland cement (OPC) was selected as the control group. The primary chemical compositions of raw coal gangue, blast furnace slag, and OPC were investigated by X-Ray fluorescence (XRF), and the results are shown in

Table 1. Compared with the chemical compositions of S95 grade granulated blast furnace slag and OPC, the coal gangue exhibited a lower CaO content and a higher SiO_2 and Al_2O_3 content, which resulted in differences in the hydration products.

Table 1. Primary chemical compositions of raw coal gangue, blast furnace slag, and cement (%).

Components	SiO_2	Al_2O_3	Fe_2O_3	SO_3	CaO	MgO	K_2O	Na_2O	Others	LOI
Coal gangue	55.14	40.96	1.23	0.43	0.41	0.30	0.20	0.09	1.24	15.33
Blast furnace slag	36.10	16.32	-	-	35.58	11.32	-	-	0.68	2.30
OPC	21.08	7.10	3.45	3.85	60.20	2.11	1.16	0.214	0.84	2.1%

The test sand and gravel were taken from Nanjing, China. The fineness modulus, apparent density, and bulk density of sand were 2.62, 2585 kg/m^3, and 1627 kg/m^3, respectively. The apparent density and bulk density of gravel were 2700 kg/m^3 and 1430 kg/m^3, respectively. In addition, the detailed gradation curves of sand and gravel by the screening test are shown in Figure 1.

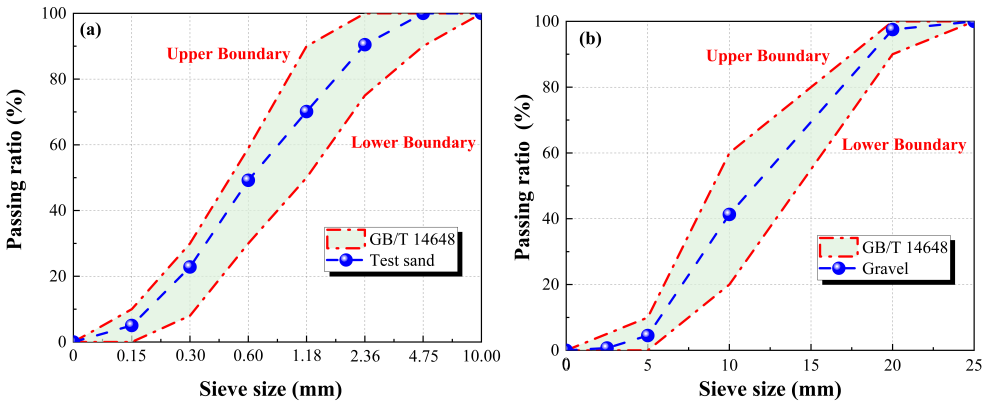

Figure 1. Gradation curve of sand (**a**) and gravel (**b**).

Previous studies have shown that sodium silicate can effectively activate the cementitious material activity of coal gangue [25,26]. Therefore, sodium silicate with a modulus of 1.2 was obtained by adding sodium hydroxide, and was employed in this research. The initial modulus of sodium silicate was 2.85, and the purity of sodium hydroxide was 99.8%.

2.2. Composite-Activated Coal Gangue

As can be seen from Table 1, the main chemical components of coal gangue are silica (SiO_2) and alumina (Al_2O_3), accounting for 96.10% of the total, which is highly similar to fly ash. However, the activity of coal gangue is low because of its overly stable crystal structure, high organic carbon, and fewer hydraulic materials [15]. Therefore, a composite activation strategy from the literature was employed to enhance the reactivity of coal gangue [20]. The results showed that the pozzolanic activity of coal gangue was at its highest when the temperature was 700 °C and the calcination time was 2 h. The procedures of the composite activation for coal gangue are shown in Figure 2. Firstly, the raw samples were crushed by a jaw crusher until the maximum particle sizes were smaller than 4.75 mm. Then, the coarse crushed particles were placed into a ball mill for grinding until milled powder passed through a 0.075 mm sieve, at which time the residue was less than 8%. Finally, the coal gangue powder was calcined at 700 °C in a muffle furnace for 2 h.

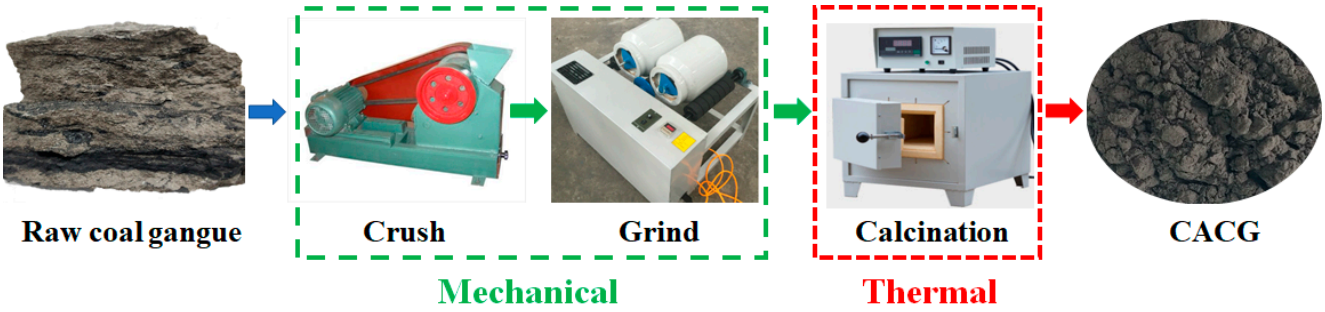

Figure 2. The composite activation procedure.

The particle size distributions of the CACG, OPC, and slag were measured by a laser particle size analyzer, the particle size distribution and parameters of which are given in Figure 3 and Table 2, respectively. The span, uniformity, D_{10}, and D_{50} of the CACG were more extensive than those of OPC and slag. The specific surface area of the CACG was smaller than that of the OPC and slag. These phenomena were attributed to the smaller average particle size of the OPC and slag. In addition, the XRD spectra of raw coal gangue and CACG are presented in Figure 4. It can be seen that coal gangue was mainly composed of kaolinite, quartz, muscovite, illite, and chlorite. The diffraction peaks of kaolinite almost disappeared after calcination at 700 °C for two hours. This phenomenon was attributed to the decomposition of kaolinite with a stable structure into amorphous silica and alumina in the thermal activation stage.

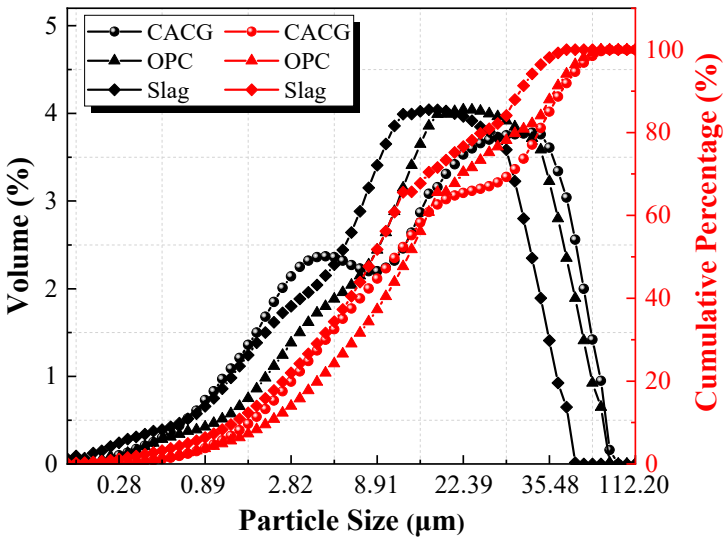

Figure 3. Particle size distributions of the CACG, OPC, and blast furnace slag.

Table 2. Parameters of the particle size distribution for the CACG, OPC, and blast furnace slag.

Parameters	Span	Uniformity	Specific Surface Area (m^2/g)	D_{10} (μm)	D_{50} (μm)
OPC	2.668	0.836	1.34	1.995	12.589
CACG	3.526	1.12	1.170	2.040	14.298
slag	2.436	0.765	1.27	1.562	11.376

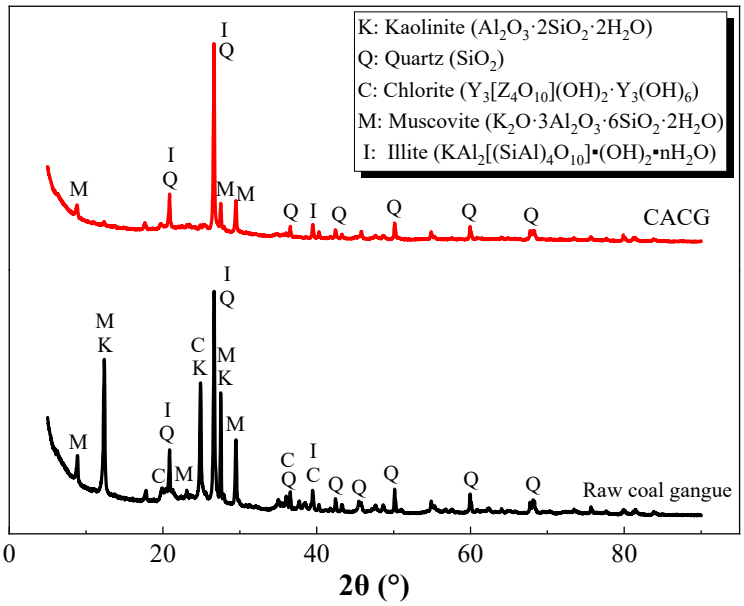

Figure 4. XRD spectra of raw coal gangue and CACG.

2.3. Mix Proportions

With reference to the JGJ 55-2011 standard [27], four groups were designed to investigate the workability, mechanical properties, and frost resistance of the AACGC with different concrete strength grades. Detailed mix proportions are listed in Table 3, where C30 indicated that the cementitious material was the OPC, and the concrete strength grade was C30; CS30 indicated that the cementitious material was the CACG and slag, and the concrete strength grade was C30.

Table 3. Mix proportions.

NO.	CACG/kg	Slag/kg	Cement/kg	Na_2SiO_3/kg	NaOH/kg	Water/kg	Sand/kg	Gravel/kg
C30	-	-	306	-	-	184	745	1165
CS30	214.2	91.8	-	71.6	27.4	184	745	1165
CS40	263.2	112.8	-	87.9	33.7	184	662	1177
CS50	312.2	133.8	-	104.3	40.0	184	584	1185

2.4. Mixing Procedures

The detailed mixing procedures used for the AACGC are summarized as follows. Firstly, the sand and gravel were dry-mixed for 2 min in a concrete mixer. Subsequently, the binders (CACG and slag) were poured into the concrete mixer and mixed for another 2 min in order to achieve homogeneity of the mixtures. Finally, the prepared alkali activator solution was added to the mixtures and stirred for another 3 min. The slump and expansion of the AACGC were measured by a slump bucket, and then the AACGC was poured into different sizes of molds. After 24 h, the molds were removed and placed in a constant temperature and humidity curing tank (the temperature is 20 ± 2 °C, and the relative humidity is 95 ± 1%) for curing to the set age.

2.5. Testing Methods

2.5.1. Slump and Slump Flow Tests

The slump and expansion test method of the Chinese code (GB/T 50164-2011) [28] was employed to determine the slump and slump flow of the AACGC. The fresh concrete was poured into the slump bucket 3 times, and a tamper bar was used to hammer evenly 25 times from the outside to the inside along the barrel wall. After pouring, the excess concrete was removed, and the slump bucket was pulled up within 5–10 s. Finally, the

difference between the height of the slump bucket and the highest point of the concrete after the collapse was measured, and this value was called the slump of concrete. The width of concrete in two directions perpendicular to each other was measured, and the average value was the called slump flow of concrete.

2.5.2. Compressive and Splitting Tests

Eighteen specimens with dimensions of 100 mm × 100 mm × 100 mm for each group were prepared in accordance with the Chinese code (GB/T 50081-2019) [29], among which nine specimens were for compressive strength at different curing times (3 d, 7 d, and 28 d), and the other nine specimens were for splitting tensile strength at different curing times (3 d, 7 d, and 28 d). A WAW-300 compression testing machine was employed to investigate the compressive strength and splitting tensile strength of the AACGC, and the loading rate was 0.5 MPa/s and 0.05 MPa/s, respectively.

2.5.3. Elastic Modulus and Axial Compressive Tests

Six specimens with dimensions of 100 mm × 100 mm × 300 mm for each group were prepared in accordance with the Chinese code (GB/T 50081-2019), among which three specimens were for elastic modulus, and the other three specimens were for axial compressive strength. The loading diagram of the elastic modulus and axial compressive tests is given in Figure 5, and the loading rate was 0.5 MPa/s. Figure 6 displays the detailed loading process of the elastic modulus, where the first loading cycles were for centering and preload. The calculation formula of the elastic modulus can be expressed as in Equations (1) and (2).

$$E_c = \frac{F_a - F_0}{A} \times \frac{L}{\Delta n} \tag{1}$$

$$\Delta n = \varepsilon_a - \varepsilon_0 \tag{2}$$

where E_c is the elastic modulus of specimens (GPa); F_a is the load value corresponding to one-third of the axial compressive strength (kN); F_0 is the load value corresponding to the stress reaching 0.5 MPa (kN); A was the compression area of specimens; L was the measurement range (mm), where L = 100 mm; Δn was the mean value of two sides deformation of specimens when loading from F_a to F_0 (mm); ε_a was the mean value of two-sided deformation of specimens at F_a (mm); ε_0 is the mean value of two-sided deformation of specimens at F_0 (mm).

Figure 5. Loading diagram of elastic modulus and axial compressive test.

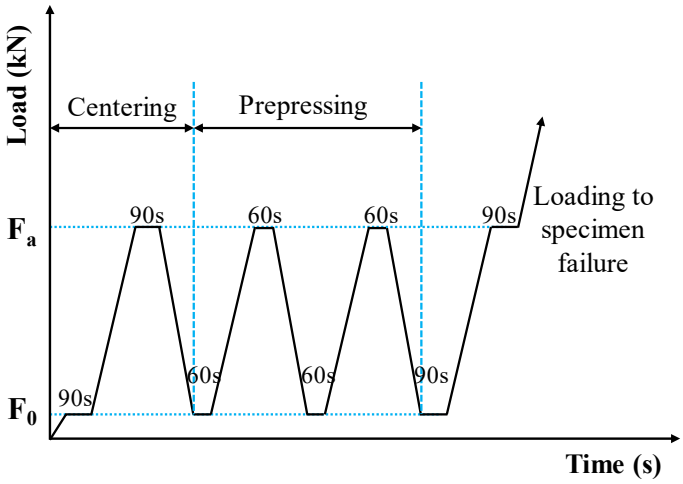

Figure 6. Loading procedure for elastic modulus.

2.5.4. Drying Shrinkage Test

In order to investigate the drying shrinkage of the AACGC, three specimens with dimensions of 100 mm × 100 mm × 515 mm for each group were prepared in accordance with the Chinese code (GB/T 50082-2009) [30]. The molds of all specimens were removed after 24 h, and were cured in a tank with a constant temperature (20 ± 2 °C) and humidity (60 ± 5%). The mass (mt) and length (Lt) of the AACGC and OPCC were recorded at 1 d, 2 d, 3 d, 4 d, 5 d, 6 d, 7 d, 14 d, 21 d, 28 d, 45 d, 60 d, 90 d, 120 d, 150 d, 180 d, and 360 d. The mass (mt) and length (Lt) results for each specimen were determined by repeated measurements three times to reduce measurement-induced errors. The mass-loss ratio ( ) and drying shrinkage ( ) of all specimens were calculated using Equations (3) and (4), respectively.

$$\triangle m = \frac{m_0 - m_t}{m_0} \times 100\% \tag{3}$$

$$\varepsilon_{st} = \frac{L_0 - L_t}{L_b} \tag{4}$$

where m_0 is the initial mass of specimens; m_t is the mass at the t-th day of specimens; L_0 is the initial length of specimens (=515 mm); L_t is the length at the t-th day of specimens.

3. Results and Discussion

3.1. Slump and Slump Flow

As can be seen from Figure 7, the slump and slump flow of the AACGC were smaller than those of the OPCC. The main reason was that the water imbibition of pozzolan cementitious materials (coal gangue and slag) was higher than that of ordinary Portland cement [21]. The CACG and slag absorbed a part of the water during the mixing process, which led to a decrease in the liquidity of the AACGC. In addition, the early hydration reaction of alkali-activated cementitious materials is faster and generates more geopolymers, resulting in a more viscous gel [31]. With the concrete strength grades of the AACGC having increased from C30 to C50, the slump and slump flow of the AACGC decreased by 33.33% and 30.26%, respectively. This was because the water-to-binder ratio gradually decreased with the increase in concrete strength grade, which led to a decrease in the liquidity of the AACGC.

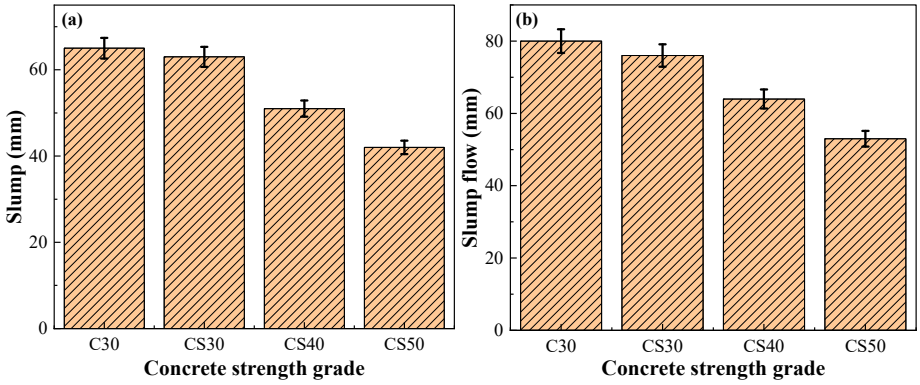

Figure 7. Slump and expansion of OPCC and AACGC: (**a**) slump; (**b**) expansion.

3.2. Mechanical Properties

3.2.1. Compressive Strength

The compressive strength, relative compressive strength, specific strength, and failure model of specimens at different curing times are shown in Figure 8, in which the specific strength is the ratio of compressive strength to mass (MPa/kg).

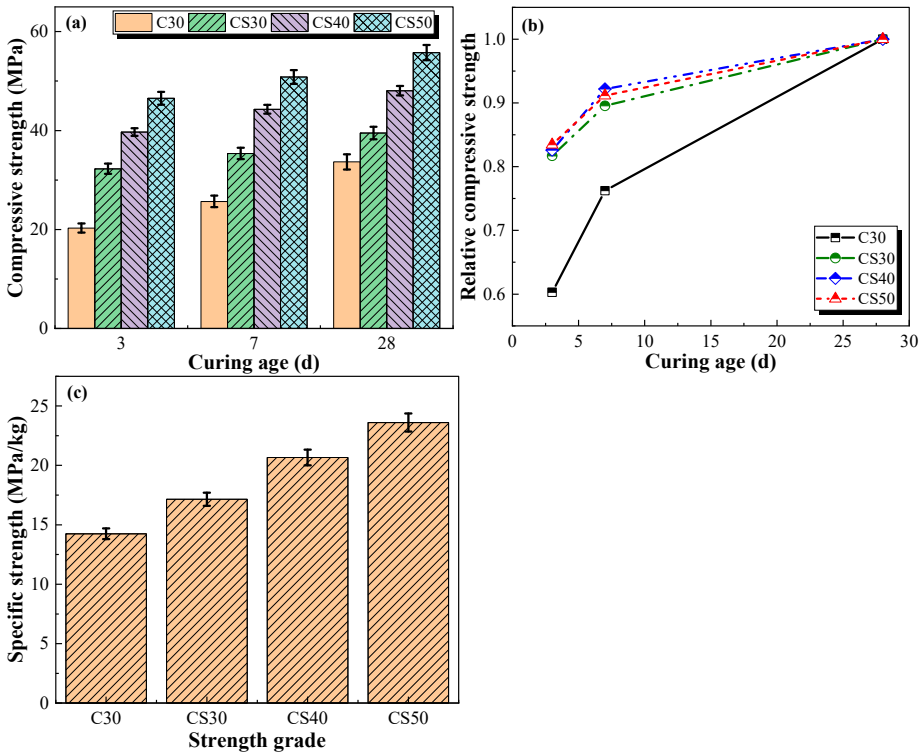

Figure 8. Comparisons of compressive performance parameters of the AACGC and OPCC: (**a**) compressive strength, (**b**) relative compressive strength, and (**c**) specific strength.

Figure 8 demonstrates that the 28 d compressive strength of the CS30 group was 1.17 times that of the C30 group, indicating that the compressive strength of the AACGC was superior to that of the OPCC. This phenomenon was attributed to the fact that the main hydration products of the AACGC were N-A-S-H gel and C-A-S-H gel, which were filled with each other in order to form a more compact structure [32,33]. As the concrete strength grade increased, the compressive strength and specific strength of specimens gradually increased. When the concrete strength grade increased from CS30 to CS50, the compressive strength and the specific strength of the CGBG concrete increased by 41.16%

and 37.67%, respectively. In addition, the failure mode of the AACGC was cone failure, which is consistent with that of OPCC.

Compared with the OPCC, the compressive strength of the AACGC increased rapidly in the first 7 d and then developed slowly after 7 d. The 3 d compressive strength of the AACGC was stable in a range of 0.81~0.83 times the 28 d compressive strength, and the 7 d compressive strength of the AACGC was stable in a range of 0.90~0.93 times the 28 d compressive strength. However, the 3 d compressive strength of the OPCC was 0.60 times the 28 d compressive strength, and the 7 d compressive strength of the OPCC was 0.76 times the 28 d compressive strength. This phenomenon can be attributed to the rapid hydration of the AACGC in the early stage.

3.2.2. Splitting Tensile Strength

The splitting tensile strength, relative splitting tensile strength, and specific strength of specimens at different curing ages are shown in Figure 9, where the specific strength is the ratio of splitting tensile strength to mass (MPa/kg).

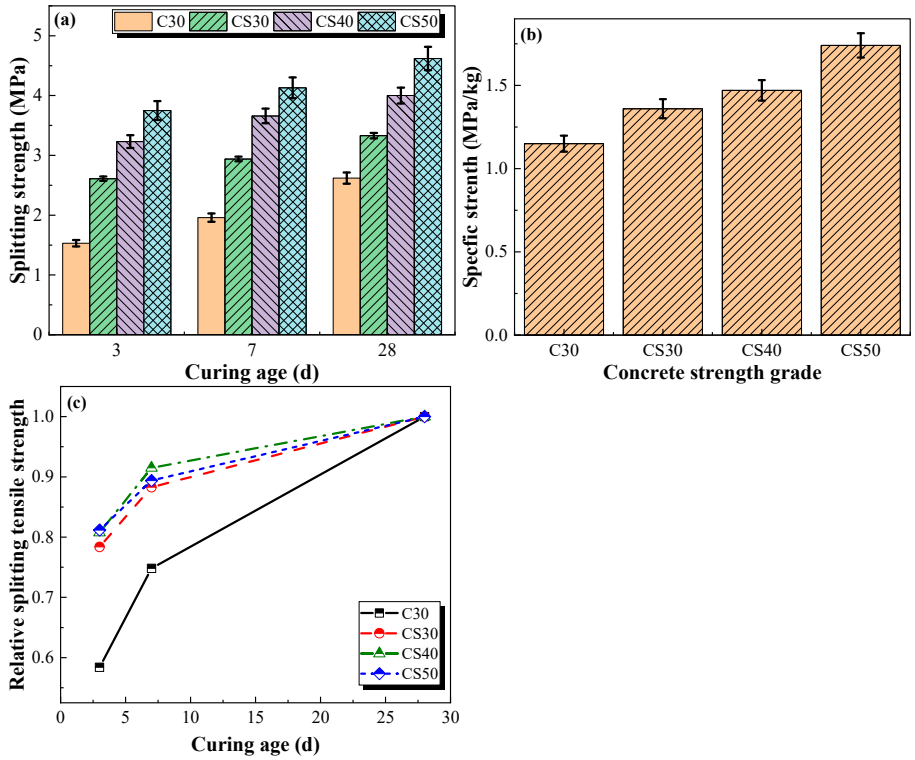

Figure 9. Comparisons of compressive performance parameters of the AACGC and OPCC: (**a**) splitting tensile strength, (**b**) specific strength, and (**c**) relative splitting tensile strength.

As displayed in Figure 9, the splitting tensile strength and specific strength of the AACGC were positively correlated with the concrete strength grade. When the concrete strength grades were changed from CS30 to CS50, the splitting tensile strength and specific strength of the AACGC increased by 38.74% and 50.05%. With the increase in concrete strength grade, the content of cementitious material and alkali activator solution increased, thus producing more hydration products with higher polymerization and density and leading to the increase in splitting tensile strength. Additionally, the 28 d splitting tensile strength and specific strength of the CS30 group were 1.27 times and 1.18 times that of the C30 group, indicating that the splitting tensile strength and specific strength of the AACGC were superior to those of the OPCC. The polymerization reactions of AACGC produce higher proportions of intersected N-A-S-H and C-A-S-H gels, and fewer proportions of orientated calcium hydroxide (CH) and needle ettringite (AFt) [32]. Therefore, the AACGC exhibited a more refined microstructure and superior mechanical properties than OPCC,

with the same water-to-binder ratio. It should be mentioned that the splitting tensile strength of the AACGC developed rapidly in the first 7 d, and then improved tardily after 7 d as the curing time continued. The 3 d splitting tensile strength of the AACGC was 78.38~81.17% of the 28 d splitting tensile strength, while the 3 d splitting tensile strength of the OPCC was 53.40% of the 28 d splitting tensile strength. Meanwhile, the 7 d splitting tensile strength of the AACGC was 88.29~91.50% of the 28 d splitting tensile strength, while the 7 d splitting tensile strength of the OPCC was 74.81% of the 28 d splitting tensile strength.

Figure 10 displays that the failure mode of the AACGC is consistent with that of OPCC. As the load value increased, cracks appeared first in the middle of the specimens, then expanded to the top and bottom to penetrate. In addition, the fracture surface was mainly the intersection of coarse aggregate and mortar. This was because the intersection of coarse aggregate and mortar was the weak zone inside the specimen.

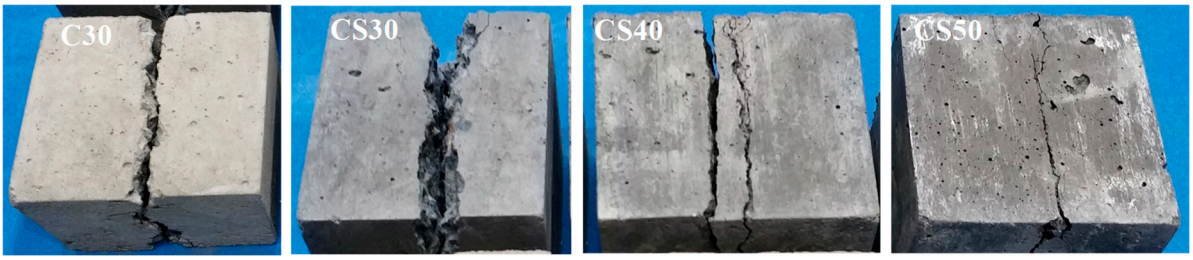

Figure 10. Failure model of specimens in compression test.

3.2.3. Ratio of Splitting Tensile strength to Compressive Strength (f_{ts}/f_c)

The ratio of the splitting tensile strength to the compressive strength (f_{ts}/f_c) for OPCC and AACGC is summarized in Figure 11. It can be seen that the average f_{ts}/f_c of the AACGC is 7.49% higher than the average f_{ts}/f_c of the OPCC, which indicates that the f_{ts} of the AACGC is superior to the f_{ts} of the OPCC. In order to further analyze the relationship between the f_{ts} and the f_c of AACGC, the previous experimental data reported in the existing literature [34–37] were applied, as plotted in Figure 12. The f_{ts} and the f_c of alkali-activated cementitious material concrete and the OPCC exhibit an excellent linear relationship. In addition, the AACGC exhibited a higher f_{ts} under the same f_c than that of the OPCC, which can be attributed to the improvement of the interface between the aggregates and the pastes. The denser hydration products of alkali-activated cementitious materials penetrated the pores of aggregates, which increased the mechanical interlocking at the aggregate–paste interface and improved the interfacial microstructures, thereby effectively enhancing the splitting tensile strength of the AACGC [34].

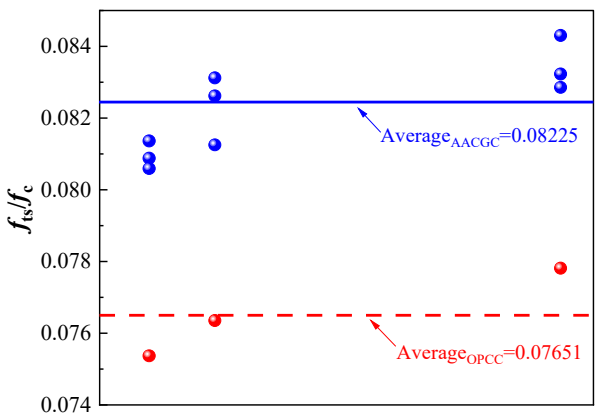

Figure 11. Ratio of the f_{ts} to the f_c of various concrete types.

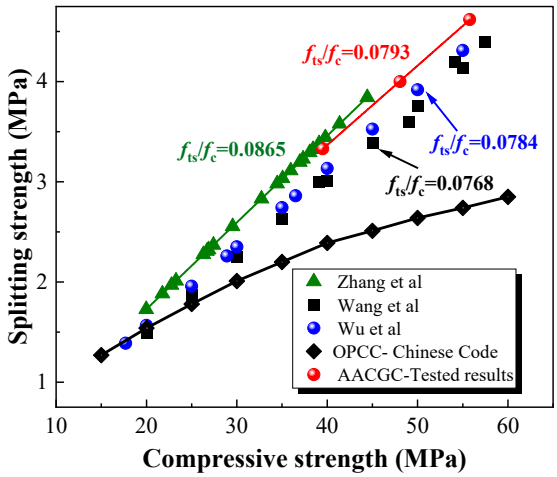

Figure 12. Relationship between the f_{ts} and the f_c of concrete [25–28].

3.2.4. Elastic Modulus

The empirical formulas of the elastic modulus and compressive strength for the OPCC in various regions codes were summarized in Table 4. These were employed to obtain the predicted value (E_{pre}) of the elastic modulus of the AACGC and OPCC, in which E_c is the elastic modulus of specimens (GPa), and $f_{cu,k}$ is the 28 d compressive strength of OPCC and AACGC (MPa). In addition, the experimental values (E_e) of the elastic modulus of specimens were calculated using Equations (1) and (2), as shown in Figure 13.

Table 4. Empirical formulas of the elastic modulus for the OPCC.

Code	Formula	Reference
GB 50010-2002	$E_c = \frac{10^5}{2.2+\frac{34.7}{f_{cu,k}}}$	[37]
ACI 318	$E_c = 4730\sqrt{f_{ck}}$	[38]
EN 1992 Eurocode 2	$E_c = 9500(f_{ck}+8)^{1/3}$	[39]
BS 8110:1997	$E_c = (20+0.2f_{cu,k}) \times 10^3$	[40]

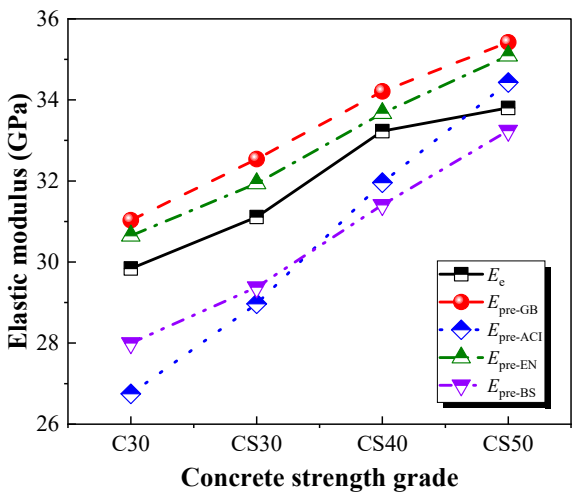

Figure 13. Comparisons between tested elastic modulus and predicted values.

As can be seen from Figure 13, the elastic modulus of the AACGC and the concrete strength grade exhibited a positive correlation. When the concrete strength grade of the AACGC increased from CS30 to CS50, the elastic modulus increased from 31.11 GPa to 33.80 GPa, with an increase of 8.68%. Compared with the C30 group, the Ee and Et of the elastic modulus of the CS30 group increased by 4.36% and 4.94%, respectively. Furthermore,

the values of the elastic modulus for AACGC and OPCC which were predicted by the empirical formula in GB 50010-2002 code and En 1922 Eurocode 2 were in good agreement with the experimental values, and the errors were within 3.50% and 3.67%, respectively. However, the predicted value of the elastic modulus obtained by the empirical formula in ACI 318 code and BS 8110:1997 code had large errors, with discrepancies of 24.71% and 21.70% with the test value, respectively. Therefore, the empirical formula of the elastic modulus in GB 50010-2002 code and En 1922 Eurocode 2 were also applicable to the AACGC.

3.2.5. Axial Compressive Strength

Figure 14a displayed that the axial compressive strength of the AACGC was higher than that of the OPCC. The 3 d, 7 d, and 28 d axial compressive strengths of the CS30 group were 2.01 times, 1.76 times, and 1.47 times those of the C30 group. This was because the intensive hydration products of alkali-activated coal gangue cementitious materials infiltrated and filled the surface pores of sand and gravel, which strengthened the interfacial transition zone (ITZ) between the aggregates and paste matrix, thereby alleviating the propagation of cracks during the loading procedure and enhancing the mechanical interaction between the paste and the aggregates [25]. Moreover, the axial compressive strength of the AACGC gradually increased as the concrete strength grade increased. When the concrete strength grades increased from CS30 to CS50, the axial compressive strength of the AACGC increased by 64.42%. The growth mechanism was similar to alkali-activated cementitious materials [21,41]. Figure 14b indicated that compared with the OPC concrete, the axial compressive strength of the AACGC developed rapidly in the first 7 d and then improved tardily after 7 d as the curing time continued. The 3 d axial compressive strength of the AACGC was 78.11~81.00% of the 28 d axial compressive strength, while the 3 d axial compressive strength of the OPCC was 55.00% of the 28 d axial compressive strength. Meanwhile, the 7 d axial compressive strength of the AACGC was 91.28~92.56% of the 28 d axial compressive strength, while the 7 d axial compressive strength of the OPCC was 75.01% of the 28 d axial compressive strength.

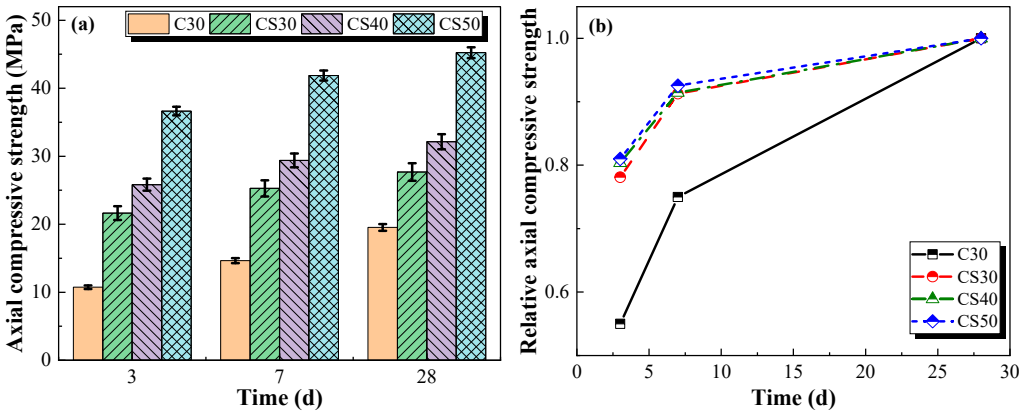

Figure 14. Comparisons of the (**a**) axial compressive strength and (**b**) relative axial compressive strength of the AACGC and OPCC.

As depicted in Figure 15, the failure mode for the OPCC and AACGC were similar, but some subtle differences also existed. The primary cracks of the OPCC and AACGC both extended along the diagonal, but the inclination angle between the cracks and the axis for the OPCC was about 25–35°, while the inclination angle between the cracks and the axis for the AACGC was about 20–30°. In addition, more cracks appeared in the AACGC, demonstrating that the interfacial transition zone (ITZ) between the Alkali-activated coal gangue cementitious material and the coral aggregates was improved [25]. During the axial compression test of the AACGC, there was a clear sound of concrete cracking, and the edge concrete kept falling off.

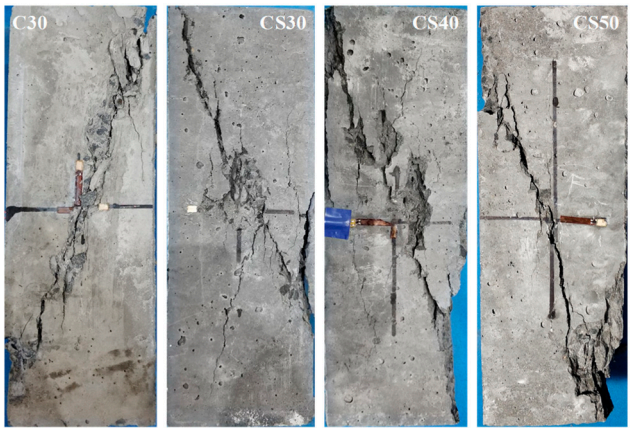

Figure 15. Failure model of specimens in axial compression test.

3.3. Drying Shrinkage

3.3.1. Mass-Loss Rate

Previous studies found that the drying shrinkage of alkali-activated cementitious materials was mainly caused by the evaporation of internal water [23]. Compared with cement-based materials, there is a large amount of free water in the alkali-activated cementitious material system. Therefore, the free water will rapidly evaporate when it is placed in a dry environment after hardening, leading to significant drying shrinkage. The mass-loss rates of the AACGC at different concrete strength grades were plotted in Figure 16, in which the OPCC was used as the control group.

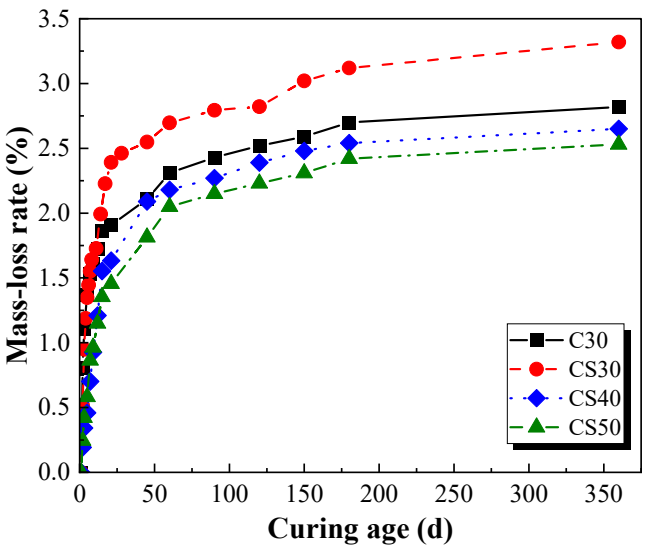

Figure 16. Mass-loss rate of the AACGC and OPCC.

Figure 16 indicates that the mass-loss rate of the AACGC and OPCC increases gradually with the increase in curing ages. It should be noticed that the mass-loss rate increased rapidly in the first 30 days, and then developed slowly. In the early stage of curing, the internal hydration reaction of specimens is fast, and the hydration heat is high, which leads to the rapid evaporation of free water and loss of mass. Moreover, the mass-loss rate of the AACGC exhibited a negative correlation with the concrete strength grade. The mass-loss rate of the CS30 group was 1.21 times and 1.30 times that of the CS40 and CS50 groups, respectively. As the concrete grade increases, the water-to-binder ratio and the free water content of the AACGC decreases gradually, leading to the reduction in the mass-loss rate. Compared with the OPCC, the mass-loss rate of the AACGC was higher. The mass-loss rate of the AACGC at 28 days, 60 days, 120 days, and 360 days was 1.29 times, 1.17 times,

1.14 times, and 1.15 times that of the OPCC. The main reason is that there is a large amount of free water in the alkali-activated cementitious material system.

3.3.2. Drying Shrinkage

As displayed in Figure 17, the drying shrinkage of each group gradually increased with the increase in curing age. It was worth noting that the trend of drying shrinkage and mass-loss rate with curing age was similar; it increased rapidly in the first 30 days and then developed slowly. This phenomenon can be attributed to the more rapid polymerization reaction that promotes the formation of gel and capillary pores, herein leading to higher porosity in the paste. Additionally, the stronger self-densification effects and connected capillary pores lead to higher capillary pressure due to migration procedures. Therefore, the dimensional stability of AACGC was inferior to the conventional normal-strength concrete, namely a higher drying shrinkage [24,42]. In addition, the drying shrinkage of the AACGC decreased gradually with the increase in concrete strength grade. After 360 days of curing, the drying shrinkage of the CS30 group was 1.16 times and 1.24 times that of the CS40 and CS50 groups, respectively. As concrete strength grade increases, the water-to-binder ratio and internal free water content of the AACGC gradually decrease, so the dry shrinkage deformation caused by evaporation of free water gradually decreases. Compared with the OPCC, the drying shrinkage of the AACGC increased by 97.87% after 360 days. This high-magnitude shrinkage of AACGC over OPCC can be attributed to the differences in the pore structure and hydration products of the pastes. The high drying shrinkage and a large number of micro-cracks caused by drying shrinkage were important factors limiting the wide application of the AACGC. Thereby, several methods for reducing drying shrinkage were recommended to be applied in the preparation of the AACGC, such as shrinkage-reducing admixture, fibers, expansive admixture, and water-retaining admixture.

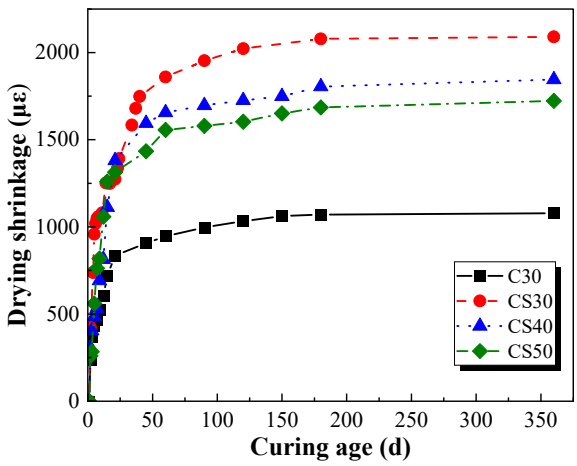

Figure 17. Drying shrinkage of the AACGC and OPCC.

3.3.3. Prediction Model of Drying Shrinkage

Extensive investigation demonstrates that the drying shrinkage of alkali-activated cementitious materials is greater than that of conventional Portland-based materials [22,41]. To date, global scholars have proposed various half-empirical prediction models to describe the drying shrinkage of the OPCC under different conditions [43–46]. Nevertheless, there is no applicable model that can accurately reflect the drying shrinkage behaviors of the AACGC. Referring to the drying shrinkage prediction models proposed by Li et al. [47], a hyperbolic prediction model was employed in the presented study, as shown in Equation (5).

$$\varepsilon_{st} = \varepsilon_{\infty} \frac{t}{t + N_s} \tag{5}$$

where ε_{st} is the drying shrinkage of specimens; ε_{∞} is the ultimate drying shrinkage of specimens; t is the curing age; a and b are the experiment constants; and N_s is the time to reach half of the ultimate drying shrinkage. The compression of the prediction results and test results of drying shrinkage for various types of concrete is displayed in Figure 18, and the difference between the prediction values (D_P) and test values (D_T) of drying shrinkage for various types of concrete at 360 days is listed in Table 5.

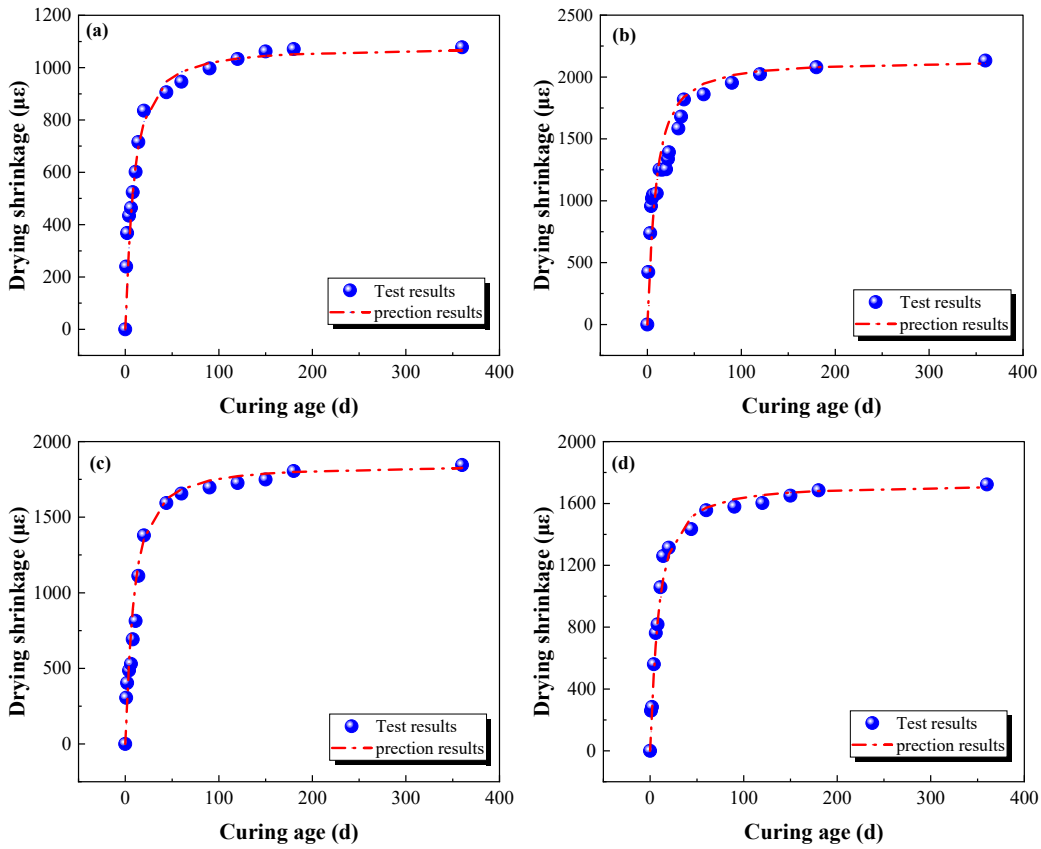

Figure 18. Comparisons of the prediction results and test results of drying shrinkage: (**a**) C30; (**b**) CS30; (**c**) CS40; (**d**) CS50.

Table 5. Difference between the D_P and D_T of drying shrinkage at 360 days.

NO.	D_T (με)	D_P (με)	D_T/D_P
C30	1078.00	1040.43	1.04
CS30	2133.00	2058.66	1.04
CS40	1845.00	1780.70	1.04
CS50	1723.00	1662.95	1.04

Figure 18 and Table 5 depict that the drying shrinkage of the AACGC predicted by Equation (5) is in good agreement with the test results, with a correlation coefficient near 0.95. In addition, the difference between the prediction values (D_P) and test values (D_T) of drying shrinkage for various concrete at 360 days was small, below 3.61%. Therefore, Equation (5) is applicable for prediction of the drying shrinkage behavior of the AACGC, with high accuracy.

4. Conclusions

This paper investigates the feasibility of using the CACG as the primary cementitious material to prepare the AACGC. The effects of concrete strength grade on flowability, mechanical properties, failure mode, and drying shrinkage of the AACGC were systematically analyzed. Several crucial conclusions could be drawn:

(1) The AACGC prepared with CACG as the primary cementitious material exhibited better mechanical properties than that of the OPCC. The compressive strength, splitting tensile strength, axial compressive strength, and elastic modulus of the AACGC were 1.17 times, 1.04 times, 1.47 times, and 1.04 times those of the OPCC, respectively. Moreover, the failure mode of axial compressive for the OPCC and AACGC were similar, but some subtle differences also existed.

(2) With the increase in concrete strength grade, the mechanical properties of the AACGC gradually increased. When the concrete strength grade increased from CS30 to CS50, the compressive strength, splitting tensile strength, elastic modulus, and axial compressive strength of the AACGC increased by 41.16%, 38.74%, 8.68%, and 64.62%, respectively.

(3) The empirical formulas of the elastic modulus and compressive strength for the OPCC in various regions codes were summarized, and the empirical formulas in GB 50010-2002 code and EN 1922 Eurocode 2 were also applicable to the AACGC.

(4) Compared with the OPCC, the AACGC has a higher mass-loss rate and drying shrinkage, which can be attributed to its rapid hydration reaction rate and high free water content. Thereby, the reduction measures were recommended to be applied in the preparation of the AACGC. The mass-loss rate and drying shrinkage gradually decrease with the increase in concrete strength grade. Additionally, the hyperbolic prediction model can accurately predict the drying shrinkage of the AACGC.

Author Contributions: Y.Z.: conceptualization, writing—original draft. C.Y.: supervision, project administration. F.Q.: writing–review and editing. K.L.: resources, data curation. J.Y.: resources, data curation. Z.W.: supervision, project administration. All authors have read and agreed to the published version of the manuscript.

Funding: This research was funded by the National Natural Science Foundation of China (52078122), the Nanjing International joint research and development project of China (2022SX00001057), and the National Key R & D Program of China (2017YFC0504505).

Institutional Review Board Statement: Not applicable.

Informed Consent Statement: Not applicable.

Data Availability Statement: The original contributions presented in the study are included in the article; further inquiries can be directed to the corresponding author.

Conflicts of Interest: The authors declare that they have no known competing financial interest or personal relationships that could have appeared to influence the work reported in this paper.

References

1. Li, Y.; Yao, Y.; Liu, X.M.; Sun, H.H.; Ni, W. Improvement on pozzolanic reactivity of coal gangue by integrated thermal and chemical activation. *Fuel* **2013**, *109*, 527–533. [CrossRef]
2. Peng, B.; Li, X.; Zhao, W.; Yang, L. Study on the release characteristics of chlorine in coal gangue under leaching conditions of different pH values. *Fuel* **2018**, *217*, 427–433. [CrossRef]
3. Kasassi, A.; Rakimbei, P.; Karagiannidis, A.; Zabaniotou, A.; Tsiouvaras, K.; Nastis, A.; Tzafeiropoulou, K. Soil contamination by heavy metals: Measurements from a closed unlined landfill. *Bioresour. Technol.* **2008**, *99*, 8578–8584. [CrossRef]
4. Li, J.Y.; Wang, J.M. Comprehensive utilization and environmental risks of coal gangue: A review. *J. Clean. Prod.* **2019**, *239*, 117946. [CrossRef]
5. Jabłońska, B.; Kityk, A.V.; Busch, M.; Huber, P. The structural and surface properties of natural and modified coal gangue. *J. Environ. Manag.* **2017**, *190*, 80–90. [CrossRef]
6. Zhao, Y.; Yang, C.; Cheng, S.; Wu, Z.; Wang, B. Performance and Hydration Mechanism of Modified Tabia with Composite-Activated Coal Gangue. *Crystals* **2022**, *12*, 150. [CrossRef]
7. Li, M.; Zhang, J.x.; Li, A.l.; Zhou, N. Reutilisation of coal gangue and fly ash as underground backfill materials for surface subsidence control. *J. Clean. Prod.* **2020**, *254*, 120113. [CrossRef]

8. Liu, H.; Xu, Q.; Wang, Q.; Zhang, Y. Prediction of the elastic modulus of concrete with spontaneous-combustion and rock coal gangue aggregates. *Structures* **2020**, *28*, 774–785. [CrossRef]
9. Frías, M.; Rojas, M.; García, R.; Valdés, A.; Medina, C. Effect of activated coal mining wastes on the properties of blended cement. *Cement Concrete Comp.* **2012**, *34*, 678–683. [CrossRef]
10. Yang, J.B.; Fang, Y.; Li, D.X. Hydration Products C-A-S-H and N-A-S-H of Alkali-activated Materials. *Bull. Chin. Ceram. Soc.* **2017**, *36*, 3292–3297, 3310. [CrossRef]
11. Purdon, A.O. The action of alkalis on blast-furnace slag. *J. Soc. Chem. Ind.* **1940**, *59*, 191–202.
12. Al Makhadmeh, W.; Soliman, A. Effect of activator nature on property development of alkali-activated slag binders. *J. Sustain. Cem-Based.* **2020**, *10*, 240–256. [CrossRef]
13. Luukkonen, T.; Yliniemi, Z.A.J.; Kinnunen, P.; Illikainen, M. One-part alkali-activated materials: A review. *Cement Concrete Res.* **2018**, *103*, 21–34. [CrossRef]
14. Zhang, P.; Guo, Z.G.J.W.J.; Hu, S.; Ling, Y. Properties of fresh and hardened fly ash/slag based geopolymer concrete: A review. *J. Clean. Prod.* **2020**, *270*, 122389. [CrossRef]
15. Zhou, M.; Wang, Z.S. Analysis of Coal Gangue Used to Produce Green Materials. *Sci. Technol. Eng.* **2007**, *7*, 1443–1445.
16. Xia, C.L.J.; Zi, G.; Yu, F.; Xie, Y. Extraction of valuable element alumina from coal gangue based on microwave assisted and response surface methodology. *Chin. J. Environ. Engin.* **2015**, *9*, 5071–5077.
17. Li, D.; Song, X.; Gong, C.; Pan, Z. Research on cementitious behavior and mechanism of pozzolanic cement with coal gangue. *Cement Concrete Res.* **2006**, *36*, 1752–1759. [CrossRef]
18. Li, H.; Sun, H.; Xiao, X.; Chen, H. Mechanical properties of gangue-containing aluminosilicate based cementitious materials. *J. Univ. Sci. Technol. Beijing Miner. Metall. Mater.* **2006**, *13*, 183–189. [CrossRef]
19. Xue, C.Z.J.; Fang, L. Mechanical properties and microstructures of alkali activated burned coal gangue cementitious material. *Kuei Suan Jen Hsueh Pao/ J. Chin. Ceram. Soc.* **2004**, *32*, 1276–1280.
20. Zhao, Y.; Yang, C.; Li, K.; Qu, F.; Yan, C.; Wu, Z. Toward understanding the activation and hydration mechanisms of composite activated coal gangue geopolymer. *Constr. Build. Mater.* **2022**, *318*, 125999. [CrossRef]
21. Ma, H.; Zhu, H.; Wu, C.; Liu, H.C.J. Study on compressive strength and durability of alkali-activated coal gangue-slag concrete and its mechanism. *Powder Technol.* **2020**, *368*, 112–124. [CrossRef]
22. Ma, H.; Zhu, H.; Wu, C.; Fan, J.; Yang, S.; Hang, Z. Effect of shrinkage reducing admixture on drying shrinkage and durability of alkali-activated coal gangue-slag material. *Constr. Build. Mater.* **2021**, *270*, 121372. [CrossRef]
23. Ma, H.; Chen, H.; Zhu, H.; Shi, Y.; Hang, Z. Study on the drying shrinkage of alkali-activated coal gangue-slag mortar and its mechanisms. *Constr. Build. Mater.* **2019**, *225*, 204–213.
24. Mastali, M.; Kinnunen, P.; Dalvand, A.; Firouz, R.M.; Illikainen, M. Drying shrinkage in alkali-activated binders–a critical review. *Constr. Build. Mater.* **2018**, *190*, 533–550. [CrossRef]
25. Zhang, B.; Zhu, H.; Li, F.; Dong, Z.; Zhang, P. Compressive stress-strain behavior of seawater coral aggregate concrete incorporating eco-efficient alkali-activated slag materials. *Constr. Build. Mater.* **2021**, *299*, 123886. [CrossRef]
26. Adam, M.J.M.H.; Ajalloeian, R.; Hajiannia, A. Preparation and application of alkali-activated materials based on waste glass and coal gangue: A review. *Constr. Build. Mater.* **2019**, *221*, 84–98.
27. *JGJ 55-2011*; Ministry of Housing and Urban-Rural Construction of the People's Republic of China. Specification for Mix Proportion Design of Ordinary Concrete. China Architecture & Building Press Beijing: Beijing, China, 2011.
28. Ministry of Housing and Urban-Rural Construction of the People's Republic of China. *Standard for Quality Control of Concrete*; China Architecture & Building Press Beijing: Beijing, China, 2012.
29. *GB/T 50081-2019*; Ministry of Housing and Urban-Rural Development of the People's Republic of China. Standard for test methods of concrete physical and mechanical properties. China Architecture & Building Press Beijing: Beijing, China, 2019.
30. *GB/T 50082-2009*; Ministry of Housing and Urban-Rural Construction of the People's Republic of China. Standard for test methods of long-term performance and durability of ordinary concrete. China Architecture & Building Press Beijing: Beijing, China, 2009.
31. Cui, C.; Peng, H.; Zhang, Y.L.J.; Cai, C.; Peng, A. Influence of GGBFS content and activator modulus on curing of metakaolin based geopolymer at ambient remperature. *J. Build. Mater.* **2017**, *20*, 535–542.
32. Cheng, Y.; Ma, H.; Wang, H.C.J.; Jing, S.; Li, Z.; Yu, M. Preparation and characterization of coal gangue geopolymers. *Constr. Build. Mater.* **2018**, *187*, 318–326. [CrossRef]
33. Ma, H.; Yi, C.; Shi, H.C.J.; Guo, Y. Property and Cementation Mechanism of Alkali-activated Coal Gangue-slag Cementitious Materials. *Cailiao Yanjiu Xuebao/Chin. J. Mater. Res.* **2018**, *32*, 898–904.
34. Zhang, B.; Zhu, H.; Wang, Q.; Shah, K.W.; Wang, W. Design and properties of seawater coral aggregate alkali-activated concrete. *J. Sustain. Cement-Based.* **2021**, *11*, 187–201. [CrossRef]
35. Wang, L.; Deng, X.; Wang, G. Experimental research on the mechanical properties of carbon fiber coral concrete. *Concrete* **2014**, *65*, 87–88.
36. Zhangyu, W.U.; Hongfa, Y.U.; Haiyan, M.A.; Zhang, Y.; Mei, Q.; Bo, D.A.; Tan, Y.; Hua, S. Study on the mechanical properties of new coral aggregate seawater concrete. *Ocean. Eng.* **2018**, *36*, 59–68.
37. Ministry of Housing and Urban-Rural Construction of the People's Republic of China. *Code for Desigin of Concrete Structures (GB 50010-2010)*; China Architecture & Building Press Beijing: Beijing, China, 2015.

38. ACI Committee. *Building Code Requirements for Structural Concrete: (ACI 318-02) and Commentary (ACI 318R-02)*; American Concrete Institute: Washington, DC, USA, 2002.
39. Européen, C. *Eurocode 2: Design of Concrete Structures—Part 1-1: General Rules and Rules for Buildings*; Standard; British Standard Institution: London, UK, 2004; p. 230.
40. Higgins, J.; Rogers, B. *Designed and Detailed (BS 8110: 1997)*; Brifish Ceiiieri Associahon (BCA): London, UK, 1998.
41. Zhang, B.; Zhu, H.; Cheng, Y.; Huseien, G.F.; Shah, K.W. Shrinkage mechanisms and shrinkage-mitigating strategies of alkali-activated slag composites: A critical review. *Constr. Build. Mater.* **2022**, *318*, 125993. [CrossRef]
42. Aydın, S.; Baradan, B. Effect of activator type and content on properties of alkali-activated slag mortars. *Compos. Part B Eng.* **2014**, *57*, 166–172. [CrossRef]
43. Gilliland, J.A. *Thermal and Shrinkage Effects in High Performance Concrete Structures during Construction*; University of Calgary: Calgary, AB, Canada, 2000.
44. ACI Committee 209. Prediction of creep, shrinkage, and temperature effects in concrete structures. *Symp. Pap.* **1982**, *27*, 51–94. Available online: https://civilmdc.com/2022/04/26/prediction-of-creep-shrinkage-and-temperature-effects-in-concrete-structures/ (accessed on 29 September 2022).
45. Bažant, Z.; Panula, L. Practical prediction of time-dependent deformations of concrete. *Matériaux Et Constr.* **1978**, *11*, 317–328. [CrossRef]
46. Gardner, N.; Lockman, M. Design provisions for drying shrinkage and creep of normal-strength concrete. *Mater. J.* **2001**, *98*, 159–167.
47. Li, K.F.; Yang, C.Q.; Huang, W.; Zhao, Y.B.; Xu, F. Effects of hybrid fibers on workability, mechanical, and time-dependent properties of high strength fiber-reinforced self-consolidating concrete. *Constr. Build. Mater.* **2021**, *277*, 122325. [CrossRef]